Angle-resolved and resonant photoemission spectroscopy study of the Fermi surface reconstruction in the charge density wave systems $CeTe_2$ and $PrTe_2$

Eunsook Lee,[1] D. H. Kim,[1] J. D. Denlinger,[2] Junwon Kim,[3] Kyoo Kim,[3] B. I. Min,[3] B. H. Min,[4] Y. S. Kwon,[4] and J.-S. Kang[1,*]

[1]*Department of Physics, The Catholic University of Korea, Bucheon 420-743, Korea*

[2]*Advanced Light Source (ALS), Lawrence Berkeley Laboratory, Berkeley, California 12345, USA*

[3]*Department of Physics, Pohang University of Science and Technology (POSTECH), Pohang 790-784, Korea*

[4]*Department of Emerging Materials Science, DGIST, Daegu 711-873, Korea*

(Received 15 November 2014; revised manuscript received 26 February 2015; published 24 March 2015)

The electronic structures of a charge density wave (CDW) system RTe_2 (R = Ce, Pr) have been investigated by employing angle-resolved photoemission spectroscopy (ARPES) and the first-principles band structure method. The R $4f$ hybridization peak ($4f^n c^{m-1}$) in the R $4f$ PES spectrum is located deeper in $PrTe_2$ than in $CeTe_2$ and R $4f$ spectral intensity near E_F is much weaker in $PrTe_2$ than in $CeTe_2$, implying the importance of the hybridization between Ce $4f$ and Te(1) $5p$ electrons. For both $CeTe_2$ and $PrTe_2$, the metallic states crossing the Fermi level (E_F) are observed below the CDW transition temperature, indicating the existence of the partially ungapped Fermi surfaces (FSs). The zigzag features having the fourfold rotational symmetry are observed near the X point in the FS of $CeTe_2$, but not in the FS of $PrTe_2$. The tight-binding model calculations show that the zigzag FS features in $CeTe_2$ can be described as the CDW-induced FS reconstruction due to the 4×4 CDW supercell structure. The effect of the linear dichroism is observed in ARPES, suggesting that the E_F-crossing states have mainly the in-plane orbital character. The photon-energy maps for the near-E_F states exhibit the straight vertical dispersions for both $CeTe_2$ and $PrTe_2$, demonstrating the dominant two-dimensional character in RTe_2 (R = Ce, Pr).

DOI: 10.1103/PhysRevB.91.125137 PACS number(s): 79.60.−i, 71.45.Lr, 71.18.+y, 71.20.−b

I. INTRODUCTION

The charge density wave (CDW) formation is one of the most interesting phenomena in solid state physics [1–3]. Transition-metal (T) dichalcogenides of TX_2 (X = S, Se) are the well-known CDW systems [4], where T d electrons play an important role in determining the CDW phenomenon. The less-studied RTe_2 (R: rare-earth ion) belongs to the p-electron CDW system, having a high CDW transition temperature of $T_{CDW} \sim 1000$ K [5–8]. RTe_2 crystallizes in the quasi-two-dimensional layered Cu_2Sb-type tetragonal structure with two types of Te sites: Te(1) and Te(2). Te(1) atoms form the planar square sheets, which are sandwiched along the c axis by the corrugated double layers of R and Te(2) atoms [6,9]. Due to the underlying R-Te(2) layer, the two-dimensional (2D) unit cell of a Te(1) sheet is doubled ($\sqrt{2} \times \sqrt{2}$), resulting in a reduced Brillouin zone (BZ) to a half of that of the Te(1) square lattice. Thereby the bands are folded into the reduced BZ to produce the shadow bands. In reality, the periodicity of the potential energy in the Te(1) layer depends on the interaction strength between Te(1) and R-Te(2) layers. Hence, the electronic structures of Te(1) sheets would keep the 2D nature of the planar square lattice if the interlayer interaction is small, while they would exhibit the three-dimensional (3D)-like nature if the interlayer interaction becomes strong.

In contrast to the triangular TX_2 (X = S, Se) CDW systems [4], the CDW states of RTe_2 are not well explored yet. The ionic configuration of RTe_2 is considered to be $R^{3+}Te(2)^{2-}Te(1)^{1-}$, which was confirmed experimentally for R = La, Ce [10]. So hole carriers are produced in Te(1) sheets. Then the square net of Te(1) are easily distorted by the Peierls-like mechanism [11] due to the partial filling. Band-structure calculations indicate that the CDW instability occurs due to the nesting between the Fermi surfaces (FSs) in Te(1) square sheets in the ab plane [5,9,12,13], which was supported by experiment [6]. The 2×2 supercell structure in the form of a double herringbone pattern [6] was reported to be a candidate CDW structure for $CeTe_2$, but the real CDW structure of $CeTe_2$ has not been confirmed either experimentally or theoretically yet. Furthermore, some electronic structure calculations indicated that the 3D nature is stronger in $CeTe_2$ than in $LaTe_2$ [12–14].

Angle-resolved photoemission spectroscopy (ARPES) is a very good experimental tool for studying the FS topology and the electronic structures of the CDW systems [4]. Despite the extensive ARPES studies for the similar CDW systems of RTe_3 [8,15,16], there are not many ARPES reports on RTe_2 [8,13,15,17,18]. Shin *et al.* [8] reported that the FS topology of $CeTe_2$ in the k_x-k_y plane is different from that of $LaTe_2$ [15], and that the magnitude of the CDW gap Δ_g varies around the FS with the minimum value of $\geqslant$600 meV, which is much larger than that found in another ARPES study ($\Delta_g \approx 100$ meV) [13,17]. Ito *et al.* [18] argued the observed intensity modulation in the FS along the k_z axis to support the strong 3D nature in $CeTe_2$. In contrast, the 3D nature is considered to be negligible in $LaTe_2$ [12,15].

Hence the following issues remain to be resolved for RTe_2: (i) What are the modulated structures after the CDW distortion? (ii) How different are the FS topology and the CDW states depending on R element? Namely, what is the role of R ions in the CDW distortion? (iii) How large is the effect of the band foldings on the FS of Te(1) sheets, arising from the interaction between Te(1) and R-Te(2) layers and the CDW supercell formation? We have resolved these questions by performing careful ARPES measurements for high-quality

*kangjs@catholic.ac.kr

stoichiometric single crystals of $R\mathrm{Te}_2$ (R = Ce, Pr), and first-principles electronic structure calculations. CeTe_2 and PrTe_2 have very similar lattice constants in agreement with the lanthanide contraction: $a = 4.47$ Å and $c = 9.11$ Å for CeTe_2 [12], and $a = 4.44$ Å and $c = 9.06$ Å for PrTe_2 [8].

II. EXPERIMENTAL AND CALCULATIONAL DETAILS

High-quality $R\mathrm{Te}_2$ (R = Ce, Pr) single crystals were grown by using the self-fluxed Bridgeman method [19]. The quality and the orientation of the single crystal were checked by Laue patterns. ARPES measurements were carried out at the MERLIN 4.0.3. beamline at the Advanced Light Source (ALS). The ARPES endstation is equipped with a Scienta R8000 electron energy analyzer and a low temperature six-axis sample manipulator cooled with an open-cycle He flow cryostat. The sample temperature can be cooled down to 6 K, but we kept the samples at ~35 K to improve their electrical conductivity. Single crystalline samples were cleaved *in situ* and measured under the pressure better than 6×10^{-11} Torr. The Fermi level (E_F) and the instrumental resolution of the system were determined from the Fermi edge spectrum of an evaporated Au metal. The photon energy ($h\nu$) corresponding to the Γ plane was determined from the photon energy scans for the Fermi-edge states at the normal emission [20]. For both CeTe_2 and PrTe_2, $h\nu \approx 108$–110 eV turned out to be close to the Γ plane within the experimental uncertainty (see Fig. 8).

For band calculations we have employed the *ab initio* full-potential linearized augmented (FLAPW) band calculations implemented in the Wien2k [21]. The generalized gradient approximation (GGA) was utilized for the exchange-correlation interaction, and the spin-orbit interaction was taken into account in the second variation manner.

III. RESULTS AND DISCUSSION

Figures 1(a) and 1(b) show the optical microscopy images of the cleaved surfaces of $R\mathrm{Te}_2$ (R = Ce, Pr) single crystals, taken after ARPES measurements. These optical images show that the ARPES data presented in this paper were obtained from the flat region because the beam size employed in ARPES measurements is less than ~40 μm. Figure 1(c) shows the angle-integrated valence-band resonant photoemission spectroscopy (RPES) spectra of CeTe_2, obtained at the Ce $4d \rightarrow 4f$ on-resonance ($h\nu = 121$ eV) and off the $4f$ resonance ($h\nu = 110$ eV), respectively. The resonance enhancement of the Ce $4f$ (between E_F and ~−5 eV) and $5p$ (between ~−18 eV and ~−22 eV) states is observed clearly. A similar resonance behavior was observed in PrTe_2 (not shown in this paper).

Figure 1(d) compares the angle-integrated valence-band RPES spectra of $R\mathrm{Te}_2$ (R = Ce, Pr), obtained at the R $4d \rightarrow 4f$ on-resonance energies. This figure reveals that both Ce and Pr $4f$ PES spectra exhibit the double-peak structures, one near E_F and the other well below E_F. The R $4f$ peaks well below E_F correspond to the trivalent R $4f^n c^m \rightarrow 4f^{n-1}c^m$ transition (c: conduction-band electron, $m = 3$). The $4f$ peaks near E_F are known to arise from the hybridization between R $4f$ and conduction-band electrons, corresponding to the $4f^n c^{m-1}$ final states [22–24]. From R = Ce to Pr, the peak positions of both the $4f^{n-1}c^m$ and $4f^n c^{m-1}$ final states shift to higher BEs. The position of the near-E_F hybridization peak ($4f^n c^{m-1}$) in R = Pr (BE ~ 1.5 eV) is deeper than in R = Ce (BE ~ 0.8 eV), and its relative intensity is much weaker than in R = Ce, resulting in the much weaker $4f$ spectral intensity near E_F. Such trends are similar to those of metallic rare-earth transition-metal compounds [25,26]. Since the metallic electronic states near E_F in the normal phase (non-CDW phase) play an important role in the CDW distortion, the observed trends from CeTe_2 to PrTe_2 indicate that the contribution from Ce $4f$ electrons to the CDW formation is stronger than that from Pr $4f$ electrons. Note, however, that the R $4f$ spectral intensity at E_F is almost negligible for both R = Ce and Pr. Hence, even if the contribution of R $4f$ electrons to the CDW exists, it would be indirect, i.e., it will contribute through the R $4f$-Te(1) $5p$ hybridization. Indeed this effect is observed in this work, which will be discussed under Fig. 2(c).

Figure 1(e) compares the Te $4d$ core-level PES spectra of $R\mathrm{Te}_2$ (R = Ce, Pr). Their line shapes are similar to each other except that the low-BE shoulder is more pronounced in PrTe_2 than in CeTe_2. Their line shapes indicate that there are several components, consistent with the presence of two different Te sites of Te(1) and Te(2) as well as the *bulk* and *surface* components for each site. We have found that the the line shapes of the Te $4d$ core-level spectra of $R\mathrm{Te}_2$ do not change much for different spots in the cleaved surfaces.

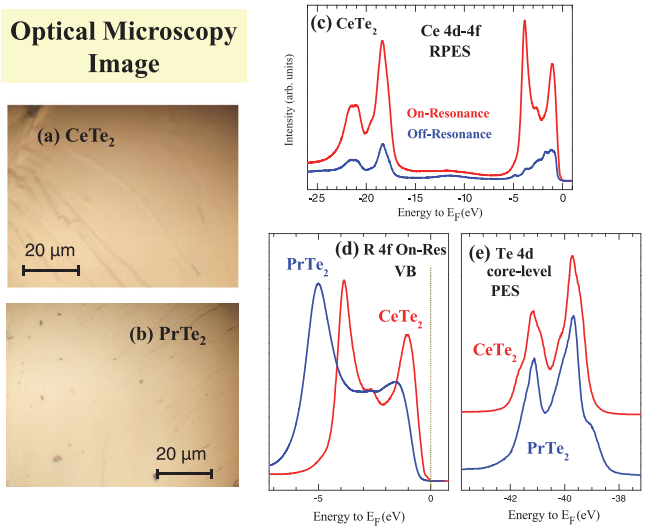

FIG. 1. (Color online) Optical microscopy images and angle-integrated PES spectra. (a) and (b) Optical microscopy images of the cleaved surfaces of $R\mathrm{Te}_2$ (R = Ce, Pr) single crystals, taken after ARPES measurements. (c) Angle-integrated valence-band R $4d \rightarrow 4f$ resonant photoemission spectroscopy (RPES) spectra of CeTe_2. Those obtained at the Ce $4f$ on-resonance energy ($h\nu = 121$ eV: red) and off the resonance energy ($h\nu = 110$ eV: blue) are compared. (d) Comparison of the angle-integrated R $4f$ on-resonance valence-band PES spectra of $R\mathrm{Te}_2$ (R = Ce, Pr). They are measured at the Ce $4f$ resonance energy ($h\nu = 121$ eV) and Pr $4f$ resonance energy ($h\nu = 124$ eV), respectively. (e) Comparison of the Te $4d$ core-level PES spectra of $R\mathrm{Te}_2$ (R = Ce, Pr), measured at $h\nu = 110$ eV. All the PES data were obtained at $T = 35$ K.

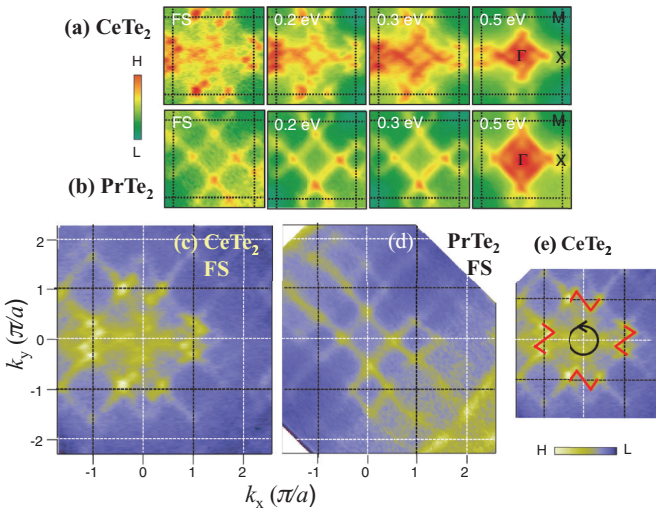

FIG. 2. (Color online) The FS and CE maps of $R\mathrm{Te}_2$ (R = Ce, Pr). (a) The constant initial-state energy (CE) maps of the ARPES intensity in the momentum space at increasing binding energies (BEs) for CeTe_2 from BE = 0 eV (E_F) to BE $\sim$ 0.5 eV (BE = $|E_i|$). Dotted lines denote the BZ. ARPES data were measured at T = 35 K and with $h\nu$ = 110 eV. (b) Similarly for PrTe_2. (c) The FS map of CeTe_2 over the wider BZ region. (d) Similarly for PrTe_2. (c) and (d) $\frac{\pi}{a}(0,0)$ and $\frac{\pi}{a}(2,0)$ correspond to the two Γ points in the first and second BZs, respectively. (e) A schematic sketch of the zigzag features near X points, drawn on top of the measured FS for CeTe_2. The ring at the center with an arrow represents the fourfold rotational symmetry of zigzag features.

Figure 2 shows the FS and constant initial-state energy (CE) maps of $R\mathrm{Te}_2$ (R = Ce, Pr). These maps correspond to the constant binding-energy (BE) slices of the angle maps between E_F ($E_F \equiv 0$ eV) and BE = 0.5 eV (BE = $|E_i|$, where E_i denotes the initial-state energy). All the FS and CE maps in this figure were obtained by integrating the spectral intensity of $E_i \pm 40$ meV for each E_i. This figure shows that the FS map of PrTe_2 is close to that of an ideal Te(1) square net, while that of CeTe_2 has the extra features in addition to that of the ideal Te(1) square net, which will be described in detail in Fig. 2(c). Nevertheless, the shapes, sizes, and energy-dependent behavior of the CE maps of CeTe_2 and PrTe_2 are similar to each other, exhibiting the fourfold rotational symmetry. The energy-dependent behavior is consistent with that of the calculated CE maps in Fig. 2 of Ref. [13].

The FSs of $R\mathrm{Te}_2$ (R = Ce, Pr), measured over the wide angle regions, are shown in Figs. 2(c) and 2(d). The CDW gaps are found to open only partially in some part of the FS, which is consistent with the semimetallic nature of $R\mathrm{Te}_2$ [17,27,28]. The overall similarity of the FS/CE maps of CeTe_2 and PrTe_2, as well as those of LaTe_2 [15], implies that the contribution of the R 4f (R = Ce, Pr) electrons to the states at E_F is minor. Nevertheless, Figs. 2(c) and 2(d) show the crucial differences between CeTe_2 and PrTe_2. The zigzag shape features are observed near the X points in the FS map of CeTe_2, while these features are absent in PrTe_2 [29]. To help to identify the zigzag features in CeTe_2, a schematic sketch of the zigzag features near X points is shown on top of the measured FS for CeTe_2 in Fig. 2(e). This finding suggests that the origin of these extra features in CeTe_2 is the hybridization between Ce 4f and Te(1) 5p states because they are not observed in PrTe_2. We also think that these X-point features in CeTe_2 arise from the CDW-induced FS reconstruction because the calculated FS maps for the non-CDW phases do not reveal these zigzag features near X (see Fig. 7).

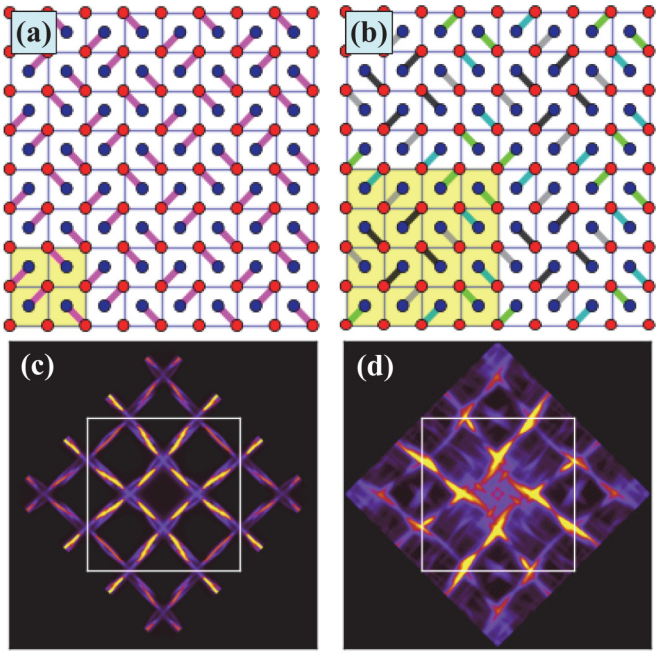

FIG. 3. (Color online) The CDW distorted unit cells and the corresponding FSs for CeTe_2. (a) The CDW supercell structure composed of a candidate 2 × 2 unit cell (yellow-colored cell) in the Te(1) sheet. Dumbells represent the dimerized Te(1) atoms in the ab plane. (b) Similarly for a candidate 4 × 4 unit cell (yellow-colored cell) in the Te(1) sheet. (c) and (d) The calculated FSs using the tight-binding models for the CDW supercell structures shown in (a) and (b), respectively. Those FSs are unfolded into the first BZ of the non-CDW phase [depicted as square boxes in (c) and (d)].

The zigzag structures near X show the fourfold symmetry, but not the mirror symmetry. These features in CeTe_2 are reminiscent of those in LaTe_2 [15]. But the zigzag features in LaTe_2 were detected for the CE map with deeper BE of $\sim$100–160 meV. As mentioned above, the zigzag features seem to arise from the CDW supercell structure in Te(1) sheets, which would yield the additional band foldings. Note, however, that this kind of zigzag features in the FS cannot be obtained for a double herringbone-type 2 × 2 supercell structure, which was suggested to be a candidate CDW structure of CeTe_2 [6].

Figure 3 shows the reported 2 × 2 and the assumed 4 × 4 supercell structures for CeTe_2, and the corresponding FSs that are obtained from the tight-binding model calculations [30]. In these calculations, the effect of the Ce 4f orbitals was taken into account in the effective Te-Te hopping parameters of the tight-binding model Hamiltonian. The FS for the 2 × 2 structure in Fig. 3(a) does not exhibit the zigzag features near X. In contrast, new features are observed near X in the FS for the 4 × 4 structure in Fig. 3(b), which are analogous to those in the measured FS. These findings indicate that the zigzag structures near X are not compatible with the reported 2 × 2 supercell structure [6] and that the CDW states in CeTe_2 might be formed as the 4 × 4 supercell structure rather than the

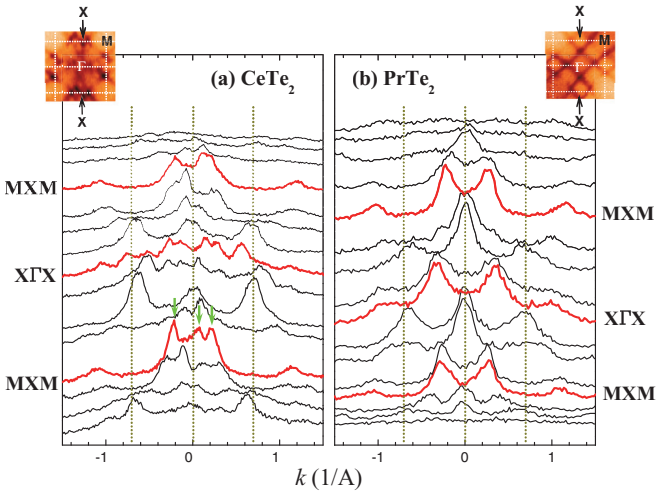

FIG. 4. (Color online) MDCs for $R\mathrm{Te}_2$ (R = Ce, Pr) along the (100) direction. (a) The MDC stack for CeTe_2 for cuts parallel to (100), obtained at $T = 35$ K and $h\nu = 110$ eV. In the MDC stack, each MDC curve is shifted vertically by a constant. The green arrows on the MDC curve represent the $\vec{k}$ points, where the states cross E_F near the X point. The inset shows the FS and the white dotted lines on the FS represent the three symmetry lines in the MDC cuts. (b) Similarly for PrTe_2.

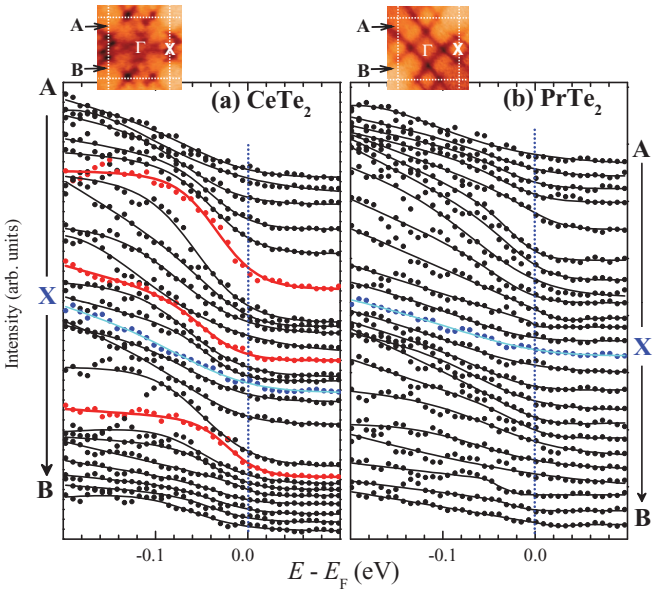

FIG. 5. (Color online) Near-E_F EDCs for $R\mathrm{Te}_2$ (R = Ce, Pr). (a) EDC stacks for CeTe_2 for a cut through the X point, i.e., the EDC stacks along the M-X-M direction, obtained at $T = 35$ K and $h\nu = 110$ eV. The solid lines, superposed on the EDCs, provide the guidelines for the EDC line shapes. The EDC in blue corresponds to that at X. The inset at the top shows the FS of CeTe_2. A and B denote the k_y points where the top and bottom EDCs are obtained. The EDCs that have stronger intensities than others are denoted in red color. (b) Similarly for PrTe_2.

2×2 structure. Note that the zigzag features in the calculated FS for the 4×4 supercell structure result from the special combination of the Peierls distortions of the crossing 1D Te chains in the 2D Te square net, as shown in Fig. 3(b). Further experimental and theoretical studies are demanded to clarify this issue.

Figure 4 shows the momentum distribution curves (MDCs) for the cuts parallel to the (100) direction in the FS maps of $R\mathrm{Te}_2$ (R = Ce, Pr), as shown in the insets. In the MDC stacks, each MDC curve is shifted vertically by a constant. These MDCs correspond to the intensity profiles of the states at E_F versus k_x for a fixed k_y value. Hence the peaks in MDCs represent the states that cross E_F at the corresponding $\vec{k}$ points. The MDC curves, depicted by thick red lines, represent those along M-X-M, X-Γ-X, and M-X-M, respectively. The MDC peaks in CeTe_2 reveal the near-X features very well, as discussed in Fig. 2(c). In order to identify the peak positions due to the zigzag shape near X in CeTe_2, green arrows are added on the MDC along M-X-M (bottom cut) of CeTe_2. In contrast, no such MDC peaks are observed in PrTe_2 around X points. The differences in the MDCs between CeTe_2 and PrTe_2 suggest that the hybridization between Ce $4f$ and Te(1) $5p$ states plays an important role in determining the CDW formation in CeTe_2 and gives rise to the extra zigzag-shape FS near X in CeTe_2.

The opening of the $\vec{k}$-dependent CDW gaps in the FS would be observed in the energy distribution curves (EDCs) as the vanishing spectral intensity near E_F. Figure 5 shows the near-E_F EDCs for the M-X-M cut in the FS maps of $R\mathrm{Te}_2$ (R = Ce, Pr). In the EDC stacks, each EDC curve is shifted vertically by a constant. Due to the very low spectral intensity near E_F in $R\mathrm{Te}_2$, the Fermi-level crossings of the near-E_F metallic states are not observed clearly in the EDCs for $R\mathrm{Te}_2$ (R = Ce, Pr). Nevertheless, the intensity modulations are very distinct between CeTe_2 and PrTe_2. The evidence for the E_F crossings in CeTe_2, corresponding to the zigzag FS features around X, is provided by the stronger intensity modulation in the EDCs for CeTe_2 than for PrTe_2. To identify the stronger intensity modulation in CeTe_2 clearly, the EDCs having strong intensities in Fig. 5(a) are denoted in red color. In contrast to PrTe_2, the strong intensity modulation in CeTe_2 yields the finite intensity at E_F at several $\vec{k}$ points, indicating no gap at the corresponding $\vec{k}$ points. Figure 5 also reveals that the magnitude of the gap varies continuously along M-X-M (along the cut through the zigzag-shaped FS). Hence the EDCs shown in Fig. 5 support the findings of both the MDCs (Fig. 4) and the measured FSs (Fig. 2).

Figure 6 shows the measured ARPES image plots of PrTe_2 along M-Γ-M (in the first BZ), obtained with two different polarizations of LH (linear horizontal) and LV (linear vertical) polarizations. The schematic drawings on the left show the configurations for LH and LV measurements. In the LH configuration, the electric field vector $\vec{E}$ of the incident photons is nearly perpendicular to the sample surface, while $\vec{E}$ is parallel to the sample surface in the LV configuration. The upper and lower layers show the wide-energy range and near-E_F ARPES image plots, respectively. Figures 6(c) and 6(f) show the differences between LH and LV ARPES data, defined as linear dichroism (LD): LD ≡ LH − LV.

The ARPES data for PrTe_2 in Fig. 6 reveal several things. (i) Many dispersive bands are observed clearly in ARPES. The large-energy-scale band structures of PrTe_2 in ARPES are very similar to those of CeTe_2 [13]. (ii) The effect of LD,

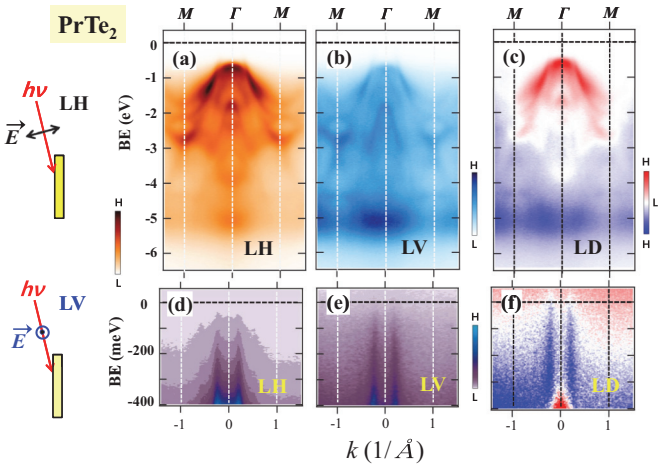

FIG. 6. (Color online) Linear dichroism (LD) in ARPES for $PrTe_2$ along M-Γ-M. (a)–(c) The measured ARPES image plots of $PrTe_2$, along M-Γ-M (in the first BZ), obtained with the linear horizontal (LH) and linear vertical (LV) polarizations, and the difference between the LH and LV ARPES, respectively, obtained at $T = 35$ K and $h\nu = 110$ eV. (d)–(f) The ARPES image plots near E_F, corresponding to the wide-energy-range ARPES of (a)–(c), respectively. Here (c) and (f) represent the LD of the ARPES. The schematic drawings on the left show the configurations for LH and LV measurements.

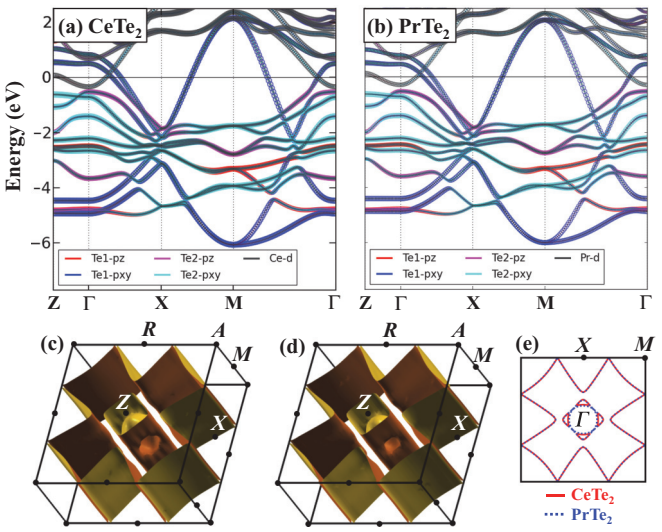

FIG. 7. (Color online) Calculated band structures of $CeTe_2$ and $PrTe_2$. (a) The calculated band structures of $CeTe_2$, where the Ce $4f$ electrons are treated as core electrons. The different colors denote the different character of the electronic states, such as Ce $4f$, Ce $5d$, Te(1) $5p$, and Te(2) $5p$ states. The sizes of the circles for each line represent the contribution of each electronic character at different $\vec{k}$ points. (b) Similarly for $PrTe_2$. (c) The calculated FS of $CeTe_2$ in the tetragonal Brillouin zone (BZ) of the non-CDW phase. Γ, X, and M represent $\vec{k} = (0,0,0)$, $\frac{2\pi}{a}(1/2,0,0)$, and $\frac{2\pi}{a}(1/2,1/2,0)$, respectively. (d) Similarly for $PrTe_2$. (e) Comparison of the calculated FSs of $CeTe_2$ and $PrTe_2$ in the Γ plane. Red and blue colors denote $CeTe_2$ and $PrTe_2$, respectively, and violet color appears when red and blue colors overlap each other.

arising from the different polarizations, is observed clearly. The states at ∼1 eV BE exhibit the stronger intensity with the LH polarization than with the LV polarization, while those at ∼5 eV BE exhibit the opposite trend, implying that the orbitals at ∼1 eV BE and at ∼5 eV are ordered mainly along the c axis and in the ab plane, respectively. On the other hand, the LD of the E_F-crossing states is opposite to the LD of the ∼1 eV BE states. The E_F-crossing bands exhibit the stronger intensity with the LV polarization than with the LH polarization, implying that the E_F-crossing orbitals are ordered mainly in the ab plane than along the c axis. (iii) The band crossing through E_F is clearly observed in the near-E_F ARPES image plots. These states are expected to produce the FSs at the corresponding $\vec{k}_F$ values.

The E_F-crossing positions, observed in ARPES, agree very well with those in the calculated bands for the non-CDW phase of RTe_2 (see Fig. 7), which have mainly Te(1) $5p$ character [12]. In the near-E_F ARPES for $CeTe_2$ [13], two crossing bands near Γ (∼0.2ΓM) and M (∼0.7ΓM) were observed, which produced the inner bright FS and outer dim FS, respectively, along Γ-M in the first BZ. The much stronger spectral weight of the former band (∼0.2ΓM), as compared to the latter band (∼0.7ΓM), was explained by the main (former) versus the shadow (latter) band nature. In contrast, in the near-E_F ARPES for $PrTe_2$, only the band near Γ (∼0.2ΓM) is observed in Figs. 6(d)–6(f). This feature is consistent with the almost vanishing outer FS of $PrTe_2$ along Γ-M in Fig. 2(d), reflecting that the 3D interaction between Te(1) and R-Te(2) layers is weak.

Figures 7(a) and 7(b) show the calculated band structures of RTe_2 (R = Ce, Pr), where R $4f$ electrons are treated as core electrons. Here the different colors denote the different character of the electronic states, such as $5p_{x+y}$ and $5p_z$ states of Te(1) and Te(2), and R $5d$. These figures reveal that the calculated band structures of $CeTe_2$ and $PrTe_2$ are very similar to each other, as expected. This is because Ce and Pr f electrons are treated as core electrons and so the R f electrons do not contribute to the electronic structures near E_F. As shown experimentally in Fig. 1(d), the Ce $4f$ states are expected to contribute more to the near-E_F electronic structures than the Pr $4f$ states. For $PrTe_2$, a very good agreement is found in the overall band structures between ARPES (Fig. 6) and calculations (Fig. 7). Especially, the calculational results of the dominant $5p_{x+y}$ character in the ab plane near E_F and at ∼5 eV BE are quite consistent with the observed LD in Fig. 6(c).

Figures 7(c) and 7(d) show the calculated FSs of RTe_2 (R = Ce, Pr) in the tetragonal BZ of the non-CDW phase. Note that the calculated FSs for $CeTe_2$ and $PrTe_2$ are very similar to each other, as shown more clearly in Fig. 7(e). No extra features are observed near the X points in the calculated FSs of $CeTe_2$, contradictory to experiment [see Fig. 2(c)]. Such discrepancy in $CeTe_2$ is expected to arise from the CDW distortion because the FSs in Fig. 7 are calculated for the non-CDW phases. The similarity between the measured FS and the calculated FS for $PrTe_2$ implies that the metallic states remain even after the CDW transition with the remnant ungapped FS and that the FS reconstruction due to the CDW transition is quite weak.

Figure 8 shows the measured and calculated FSs in the k_x-k_z plane for RTe_2 (R = Ce, Pr). Figure 8(a) shows the measured

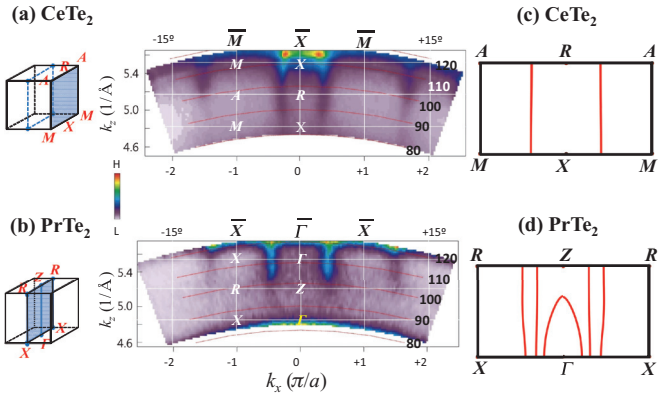

FIG. 8. (Color online) Photon energy map. (a) The Fermi-edge state $h\nu$ map for $CeTe_2$ for $h\nu$ between 80 and 120 eV, obtained at $T = 35$ K. Horizontal k_x direction is parallel to (100) and cuts through $M(A)$-$X(R)$-$M(A)$ along k_z ($h\nu$). (b) Similarly for $PrTe_2$ for k_x through $X(R)$-$\Gamma(Z)$-$X(R)$. (c) The calculated FS for the k_x-k_z BZ in $CeTe_2$. (d) Similarly for $PrTe_2$.

Fermi-edge $h\nu$ (k_z) maps between 80 and 120 eV with the horizontal direction along (100). So these maps show the FSs in the k_x-k_z plane. The k_x-k_z ($h\nu$) map for $CeTe_2$ is obtained for the BZ of MXM-ARA, and that for $PrTe_2$ is for the BZ of $X\Gamma X$-RZR. For $CeTe_2$, the MXM-ARA cut is chosen because the zigzag-type features, present around X in the measured FS for $CeTe_2$ [Fig. 2(c)], are expected to be observed along M-X-M. In the $h\nu$ maps for both $CeTe_2$ and $PrTe_2$, the E_F-crossing states exhibit straight vertical dispersions along k_z. These features indicate that they originate from the $2D$-like states, and that the interaction between Te(1) and R-Te(2) layers does not have a crucial contribution to the electronic states responsible for the CDW formation in RTe_2. The bright feature is observed in $CeTe_2$ around X for $h\nu \sim 110$–115 eV, which reflects the existence of several E_F-crossing states due to the zigzag-type FS features around the X point. The calculated FS of $CeTe_2$ in Fig. 8(c) also shows the straight vertical dispersions along k_z. In the calculated FS of $PrTe_2$ [Fig. 8(d)], however, there is an extra FS centered at Γ, which is not detected in the measured FS [Fig. 8(b)]. The existence of this FS remains to be checked more carefully.

IV. CONCLUSIONS

The overall shapes and sizes of the measured FSs of RTe_2 (R = Ce, Pr) are similar to each other and they agree well with the calculated FSs for the normal-phase RTe_2. However, the zigzag-shaped features, having the fourfold rotational symmetry, are observed near the X points in the FS map of $CeTe_2$ only, but not in $PrTe_2$, suggesting that these features are due to the hybridization between Ce $4f$ and Te(1) $5p$ electrons. According to the tight-binding model calculations, these zigzag FS features in $CeTe_2$ reflect the CDW-induced FS reconstruction due to the 4×4 supercell structure. The partially ungapped FSs, measured below the CDW transition, reflect that the metallic states remain even below the CDW transition for both R = Ce and R = Pr. The effect of the LD is observed in ARPES. The E_F-crossing states are stronger with the LV polarization than with the LH polarization, suggesting that the E_F-crossing states have mainly the ab-plane orbital character.

We have found the following answers to the questions addressed in the beginning: (i) The CDW modulation of Te(1) sheets is large for $CeTe_2$, but negligible for $PrTe_2$. The CDW modulated structure for $CeTe_2$ is likely to be the 4×4 structure [see Fig. 3(b)], but not compatible with the previously reported 2×2 double herringbone structure. (ii) The R $4f$ states in RTe_2 do not contribute directly to the CDW formation, but the R $4f$-Te $5p$ hybridization is much weaker in $PrTe_2$ than in $CeTe_2$, which is reflected as the much weaker $4f$ spectral intensity near E_F in $PrTe_2$. (iii) The opposite effects of the LD are observed between the E_F-crossing states and the states at $\sim$1 eV BE, indicating that the E_F-crossing orbitals are ordered mainly in the ab plane. (iv) The $\vec{k}$-dependent energy gap $\Delta_g(\vec{k})$ was observed. (v) The straight vertical dispersions along k_z are observed in the $h\nu$ maps for the E_F-crossing states along k_z for both $CeTe_2$ and $PrTe_2$. These features demonstrate the dominant 2D character for the states near E_F.

ACKNOWLEDGMENTS

This work was supported by the National Research Foundation (NRF) under Contracts No. 2014R1A1A2056546 and No. 2011-0025237, the POSTECH-BSRI grant, and the Korea Institute of Science and Technology Information (KISTI) supercomputing center (No. KSC-2013-C3-010). The ALS is supported by US DOE under Contract No. DE-AC02-05CH11231. Y.S.K. and B.H.M. were supported by the Basic Science Research Program of the NRF (2013R1A1A2009778) and the Leading Foreign Research Institute Recruitment Program (Grant No. 2012K1A4A3053565). The travel for the ARPES experiment at the ALS was supported in part by the Ministry of Science, ICT and Future Planning (MSIP) and Pohang Accelerator Laboratory (PAL) in Korea.

[1] J. Voit, L. Perfetti, F. Zwick, H. Berger, G. Margaritondo, G. Grüner, H. Höchst, and M. Grioni, Science **290**, 501 (2000).
[2] T. Kasuya, M. H. Jung, and T. Takabatake, J. Magn. Magn. Mater. **220**, 235 (2000).
[3] T. Yokoya, T. Kiss, A. Chainani, S. Shin, M. Nohara, and H. Takagi, Science **294**, 2518 (2001).
[4] K. Rossnagel, J. Phys.: Condens. Matter **23**, 213001 (2011), and references therein.
[5] E. DiMasi, B. Foran, M. C. Aronson, and S. Lee, Phys. Rev. B **54**, 13587 (1996).
[6] K. Stöwe, J. Alloy Compd. **307**, 101 (2000); J. Solid State Chem. **149**, 155 (2000).
[7] M. H. Jung, T. Ekino, Y. S. Kwon, and T. Takabatake, Phys. Rev. B **63**, 035101 (2000).
[8] K. Y. Shin, V. Brouet, N. Ru, Z. X. Shen, and I. R. Fisher, Phys. Rev. B **72**, 085132 (2005).
[9] A. Kikuchi, J. Phys. Soc. Jpn. **67**, 1308 (1998).
[10] J.-S. Kang, C. G. Olson, Y. S. Kwon, S. W. Han, K. H. Kim, A. Sekiyama, S. Kasai, S. Suga, and B. I. Min, J. Phys.: Condens. Matter **16**, 9163 (2004).

[11] J. K. Burdett and S. Lee, J. Am. Chem. Soc. **105**, 1079 (1983).
[12] J. H. Shim, J.-S. Kang, and B. I. Min, Phys. Rev. Lett. **93**, 156406 (2004).
[13] J.-S. Kang, D. H. Kim, H. J. Lee, J. Hwang, H.-K. Lee, H.-D. Kim, B. H. Min, K. E. Lee, Y. S. Kwon, J. W. Kim, K. Kim, B. H. Kim, and B. I. Min, Phys. Rev. B **85**, 085104 (2012).
[14] K. E. Lee, B. H. Min, J.-S. Rhyee, J. N. Kim, J. H. Shim, and Y. S. Kwon, Appl. Phys. Lett. **101**, 143901 (2012).
[15] D. R. Garcia, G.-H. Gweon, S. Y. Zhou, J. Graf, C. M. Jozwiak, M. H. Jung, Y. S. Kwon, and A. Lanzara, Phys. Rev. Lett. **98**, 166403 (2007).
[16] V. Brouet, W. L. Yang, X. J. Zhou, Z. Hussain, N. Ru, K. Y. Shin, I. R. Fisher, and Z. X. Shen, Phys. Rev. Lett. **93**, 126405 (2004); V. Brouet, W. L. Yang, X. J. Zhou, Z. Hussain, R. G. Moore, R. He, D. H. Lu, Z. X. Shen, J. Laverock, S. B. Dugdale, N. Ru, and I. R. Fisher, Phys. Rev. B **77**, 235104 (2008), and references therein.
[17] J.-S. Kang, C. G. Olson, Y. S. Kwon, J. H. Shim, and B. I. Min, Phys. Rev. B **74**, 085115 (2006).
[18] T. Ito, H. J. Im, S. Kimura, and Y.-S. Kwon, J. Magn. Magn. Mater. **310**, 431 (2007).
[19] B. H. Min, H. Y. Choi, and Y. S. Kwon, Physica B **312-313**, 203 (2002); **312-313**, 205 (2002).
[20] J. D. Denlinger, J. W. Allen, J.-S. Kang, K. Sun, B. I. Min, D.-J. Kim, and Z. Fisk, J. Phys. Soc. Jpn. Conf. Proc. **3**, 017038 (2014).
[21] H. J. F. Jansen and A. J. Freeman, Phys. Rev. B **30**, 561 (1984); P. Blaha *et al.*, *WIEN2k* (Karlheinz Schwarz, Techn. Universität Wien, Austria, 2001).
[22] O. Gunnarsson and K. Schönhammer, Phys. Rev. B **28**, 4315 (1983); **31**, 4815 (1985); K. A. Gschneidner, L. Eyring, and S. Hüfner (eds.), *Handbook on the Physics and Chemistry of Rare Earths* (North Holland, Amsterdam, 1987), Vol. 10, p. 103.
[23] J. W. Allen, S.-J. Oh, O. Gunnarsson, K. Schönhammer, M. B. Maple, M. S. Torikachvili, and I. Lindau, Adv. Phys. **35**, 275 (1987).
[24] B. I. Min, H. J. F. Jansen, T. Oguchi, and A. J. Freeman, Phys. Rev. B **33**, 8005 (1986).
[25] J.-S. Kang, J. H. Hong, J. I. Jeong, S. D. Choi, C. J. Yang, Y. P. Lee, C. G. Olson, B. I. Min, and J. W. Allen, Phys. Rev. B **46**, 15689 (1992).
[26] J.-S. Kang, J. H. Hong, D. W. Hwang, J. I. Jeong, S. D. Choi, C. J. Yang, Y. P. Lee, C. G. Olson, K. C. Kang, and B. I. Min, Phys. Rev. B **49**, 16248 (1994).
[27] M. Lavagnini, A. Sacchetti, L. Degiorgi, K. Y. Shin, and I. R. Fisher, Phys. Rev. B **75**, 205133 (2007).
[28] K. E. Lee, C. I. Lee, H. J. Oh, M. A. Jung, B. H. Min, H. J. Im, T. Izuka, Y. S. Lee, S. Kimura, and Y. S. Kwon, Phys. Rev. B **78**, 134408 (2008).
[29] The polarization of the incident light is not the origin of the zigzag features near X points in $CeTe_2$ because these features are also observed when the sample is rotated azimuthally by 45°.
[30] K. Kim *et al.* (unpublished).